

Diagrammatic Monte Carlo for finite systems at zero temperature

Stefano Brolli^{1,2,*} Carlo Barbieri^{1,2,†} and Enrico Vigezzi^{2,‡}

¹*Dipartimento di Fisica “Aldo Pontremoli”, Università degli Studi di Milano, Milan 20133, Italy*

²*INFN, Sezione di Milano, Milan 20133, Italy*

(Dated: January 17, 2025)

High-order virtual excitations play an important role in microscopic models of nuclear reactions at intermediate energies. However, the factorial growth of their complexity has prevented their consistent inclusion in *ab initio* many-body calculations. For infinite systems at finite temperature, such drawbacks can be overcome using diagrammatic Monte Carlo (DiagMC) techniques to resum entire series of Feynman diagrams. We present a DiagMC algorithm that can be applied to self-bound systems with discrete energy levels at zero temperature, and demonstrate its potential for the Richardson model of nuclear pairing. We show that sampling the topological space of diagrams allows the inclusion of high-order excitations that are neglected in state-of-the-art approximations used in nuclear physics and quantum chemistry. We propose that sampling the diagrammatic space can overcome the long-standing gap between our microscopic understanding of structure and reactions in nuclear physics.

Ab initio nuclear theory has significantly advanced over the past two decades by combining effective field theories (EFT) of the nuclear force with the latest computational approaches to the quantum many-body problem. Several high-precision methods can predict the ground state properties of medium-light nuclei [1, 2], and recently reached heavy elements [3, 4]. The EFT interactions used in modern literature are rooted in the symmetries of QCD and avoid relying on the phenomenology of stable nuclei, so that controlled and accurate predictions remain feasible even toward the limits of nuclear existence. Exotic neutron-rich nuclei far from stability are essential for studying many fundamental open problems of modern physics, such as the evolution of the shell structure and the formation of heavy elements [5, 6]. In particular, the role of unstable nuclei in the astrophysical r-process in neutron star mergers cannot be overestimated [7, 8]. State-of-the-art and future facilities that work with unstable beams rely on nuclear reaction models to discover new isotopes and interpret experimental results [9–15]. Despite the success of the structure calculations discussed above, the microscopic description of nuclear reactions is more challenging [16]. Among the available *ab initio* methods [17–21], the self-consistent Green’s function (SCGF) approach is suited for a unified description of structure and reactions because of the wealth of physical information contained. The exact spectral distribution (which gathers all one-nucleon addition and removal spectroscopy), the ground-state energy and density profiles, and the exact microscopic optical potential are consistently included in the formalism [22–25]. The Green’s function G is the exact solution of the Dyson equation $G_{\alpha\beta}(\omega) = G_{\alpha\beta}^{(0)}(\omega) + \sum_{\gamma\delta} G_{\alpha\gamma}^{(0)}(\omega) \Sigma_{\gamma\delta}^*(\omega) G_{\delta\beta}(\omega)$, where $G^{(0)}$ describes a freely propagating particle (or hole) and the term $G^{(0)}\Sigma^*G$ introduces recursive dynamic interactions with the other particles of the system. In this picture, the self-energy Σ^* is a complex, nonlocal, energy-dependent microscopic optical potential

[22, 23, 26]. SCGF theory relies on systematically improvable many-body truncations of the self-energy [27], however, current approximation schemes do not include high-order configurations that dominate mid-energy scattering [19]. Due to the factorial growth of the Feynman diagrams (see Fig. 1), improving the accuracy of *ab initio* optical potentials requires to go beyond order-by-order addition of terms and to aim for a stochastic resummation by sampling a limited number of representative higher order diagrams.

Sampling different diagram topologies is the fundamental idea of the diagrammatic Monte Carlo (DiagMC) approach [29]. This method has first gained much interest in the field of condensed matter physics, where it was employed to study infinite systems at finite temperature such as the polaron [30] and the unitary Fermi gas [31, 32]. More recent advances in the DiagMC frame-

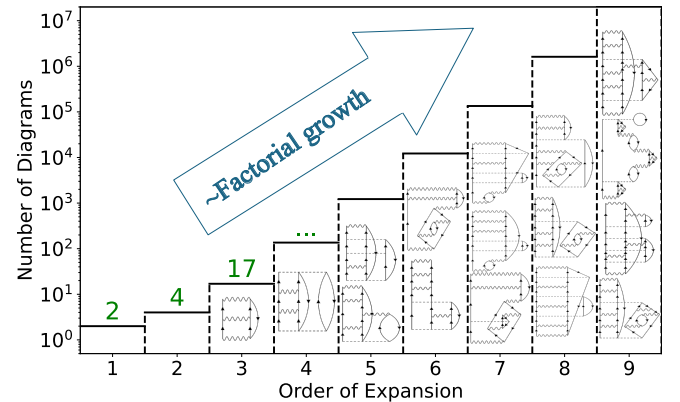


FIG. 1. Approximate number of Feynman diagrams contributing to the self-energy for two and three-body forces. The values shown in green give the exact number of Feynman diagrams for the first three orders [28] while value at higher order are estimated based on their factorial scaling. For each order, very few representative diagrams are shown.

work have been applied to study single-particle excitations in the electron gas [33, 34] and the real-time dynamics of dissipative quantum impurity models [35]. To our knowledge, DiagMC has still been poorly investigated for bound systems at zero temperature such as atomic nuclei, where (large) discrete bases are usually needed. Furthermore, applications to scattering theory require satisfying the causality principle, which is encoded in a dispersive spectral relation. This property is naturally broken by sharp truncations in the Feynman perturbation series, and it has never been enforced in previous DiagMC calculations. In this Letter, we introduce a DiagMC algorithm for the Richardson model and impose the correct dispersive relation by representing the stochastic self-energy with a parameterization suitable for finite systems.

The *Richardson model* was introduced as a simplified description of nuclear superfluidity. It explains pairing correlations in Sn and Pb isotopes with considerable accuracy [36, 37], as well as in quantum chemistry systems [38]. Furthermore, it provides stringent tests for quantum many-body theories that aim to describe strongly correlated Fermi liquids [39], and has challenged quantum neural networks [40] and eigenvector continuation [41]. The availability of exact solutions makes it suitable for precise benchmarks.

The Richardson Hamiltonian includes a contact interaction between nucleons that occupy the same energy level [42]. We consider D doubly degenerate and equidistant energy levels and we focus on the half-filled system with $A = 2P$ fermions,

$$H^{(D)} = \xi \sum_{p=1}^D \sum_{s=\uparrow,\downarrow} (p-1) c_{ps}^\dagger c_{ps} - \frac{g}{2} \sum_{p,q=1}^D c_{p\uparrow}^\dagger c_{p\downarrow}^\dagger c_{q\downarrow} c_{q\uparrow}, \quad (1)$$

where we set $\xi = 1$ without loss of generality. The ground state of this Hamiltonian can be written analytically as the product of the P lowest correlated-pair creation operators, b_i^\dagger , such that $|\Psi_0^A\rangle = \prod_{i=1}^P b_i^\dagger |0\rangle$ [43].

The propagator theory of the Richardson model was explored in Refs. [27] and [44]. The one-body propagator is diagonal and invariant under spin exchange, and hence only its D diagonal and spin-up components need to be considered. Furthermore, we found that ladder diagrams greatly dominate the self-energy expansion of the propagator in the perturbative regime. We will focus on this subset of diagrams in our sampling and show that this is sufficient to compute the full correlation energy within the stochastic error and the error induced by a finite regulator.

Diagrammatic Monte Carlo. Standard Monte Carlo integration has been used to compute many-body perturbation theory (PT) for nucleonic matter reaching up to the full fourth order [45] but relies on the cumbersome determination and evaluation of every single PT contribution [46]. The DiagMC framework used in this work overcomes this limitation by promoting diagram topolo-

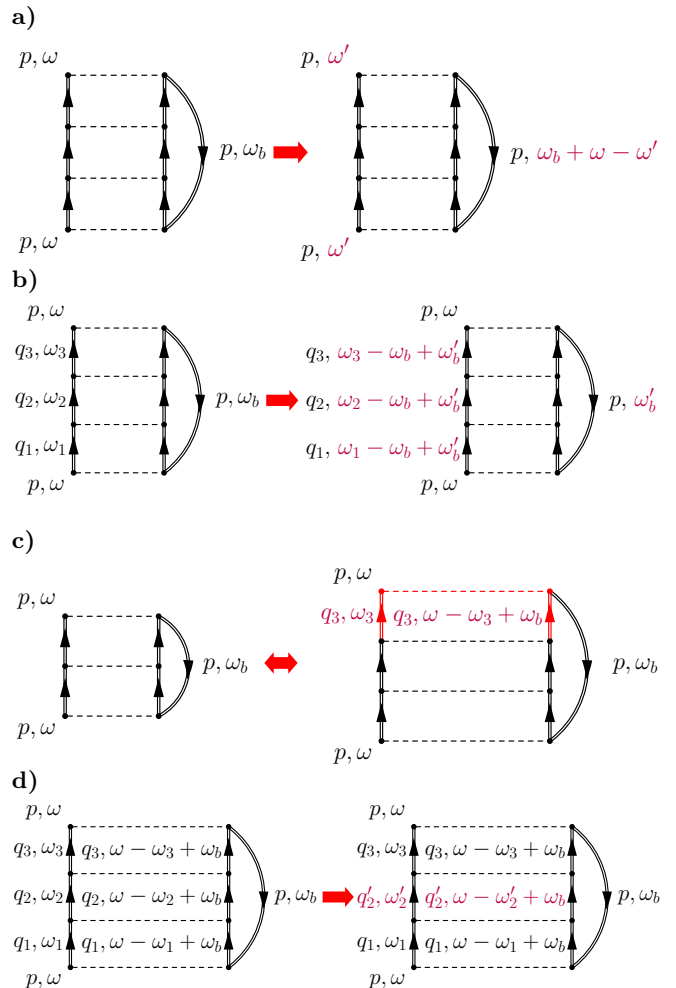


FIG. 2. Updates used to sample the entire ladder diagrammatic expansion [43]. Rules a), b) and d) yield the standard Monte Carlo evaluation of single diagrams. Rule c) allows to span the topological space of all self-energy ladder diagrams.

gies on the same footing as internal quantum numbers and frequencies [29, 31]. We express the exact self-energy according to the fundamental identity

$$\Sigma_p^*(\omega) = Z_p \int d\mathcal{C} \frac{|\mathcal{D}_p(\omega; \mathcal{C})|}{Z_p} \exp[i \arg \mathcal{D}_p(\omega; \mathcal{C})], \quad (2)$$

where \mathcal{D}_p is a diagram characterized by its topology and internal single-particle quantum numbers and frequencies, which we collectively label \mathcal{C} , and Z_p is a normalization factor. The integral over $d\mathcal{C}$ includes the sum over all topologies. If the diagrams are sampled according to a probability distribution $\propto |\mathcal{D}_p(\omega; \mathcal{C})|$, the self-energy can be calculated as a stochastic sum of the phases of the diagrams. The sampling of ladder diagrams is implemented through a Markov chain in the space of diagrams. At each step of the chain, one of the updates in Fig. 2 is called at random, and a walker in \mathcal{C} -space is generated using the Metropolis-Hastings algorithm [47, 48]. We refer to the Supplemental Material for a comprehensive overview of

the present DiagMC implementation [43].

The DiagMC algorithm is built upon the Feynman perturbation expansion which, if truncated sharply at each order, can break important non-perturbative features of the exact self-energy. Most notably, the causality principle that is important for scattering events may require full all-order summations. Causality is expressed through the boundary condition of the Källén-Lehmann representation for the exact self-energy:

$$\Sigma_{p\uparrow}^*(\omega) = \Sigma_p^{(\infty)} + \sum_{n=1} \frac{A_p^n}{\omega - B_p^n + i\eta} + \sum_{k=1} \frac{A_p^k}{\omega - B_p^k - i\eta}, \quad (3)$$

with $A_p^{n/k} > 0$. Note that the dispersion relation implies that only the static mean-field term, $\Sigma_p^{(\infty)}$, and the imaginary part of (3) are required to reconstruct the entire self-energy [25]. The algebraic diagrammatic construction (ADC) that is state-of-the-art for nuclear physics and quantum chemistry was developed with the specific aim of retaining this structure exactly [27, 49, 50].

The $\Sigma_p^{(\infty)}$ term is a tadpole diagram that plays a special role in the DiagMC algorithm. Its expression includes a convergence factor $e^{i\omega\eta}$ that makes the Monte Carlo integration inefficient; however, it can be easily calculated with standard numerical methods. Moreover, DiagMC calculates the self-energy only up to the overall (real) factor Z_p of Eq. (2). To fix this ambiguity and at the same time address the convergence problem of the tadpole diagrams, we approached the problem in a novel way. First, the $\Sigma_p^{(\infty)}$ diagram, and any diagram that includes repetitions of it, are simple enough that they can be evaluated exactly with an analytical frequency integration followed by standard integration over the remaining single-particle quantum numbers. Hence, we compute it separately to avoid any Monte Carlo instability. Second, the Markov chain walker of DiagMC can still be implemented to retain all steps over the tadpole diagrams: simply such contributions are ignored in the sum of Eq. (2) to avoid any double counting. This fact gives us the additional freedom needed to determine the overall normalization. We replace the tadpoles diagrams with unphysical ones that have an exactly known analytical solution and compare it with the partial DiagMC resummation over the same terms. We can deduce the overall normalization factor by counting how many times the unphysical diagram is visited compared to the total number of samples [43].

Within the radius of convergence for the perturbation expansion, an increase in the truncation order must bring the simulation closer to the correct Källén-Lehmann representation. An important novelty in our approach is to perform a nonlinear least-square minimization (NLLSM) that fits the imaginary part of the self-energy calculated with DiagMC as a sum of Lorentzians. Dispersion re-

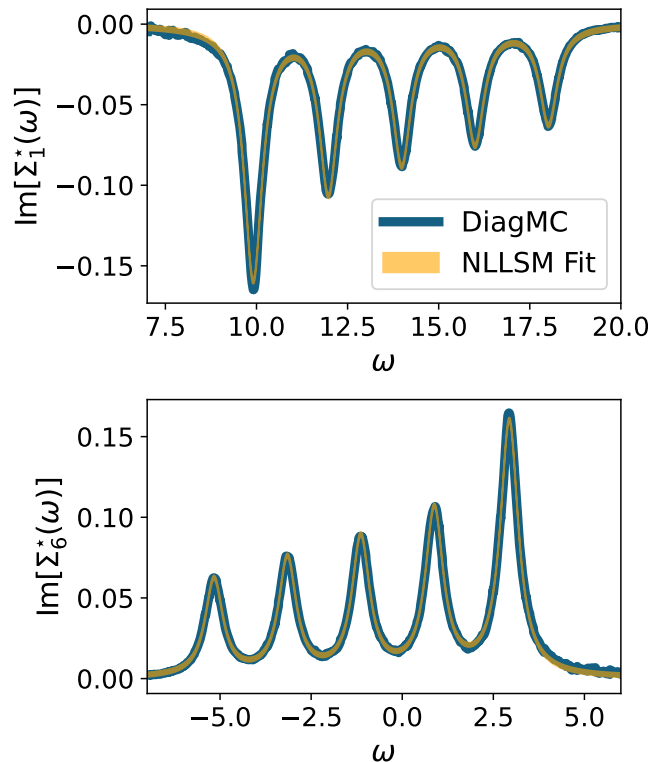


FIG. 3. Imaginary part of the diagonal components $p = 1, 6$ of the irreducible self-energy. The self-energy was calculated with DiagMC and fitted via NLLSM with a sum of Lorentzian functions. The simulation was performed with a HF reference propagator in a model space of dimension $D = 10$ and $A = 10$ particles. We used $g = 0.3$, $\eta = 0.1$. DiagMC sampled the ladder series up to the eighth order. The Lorentzian representation is very accurate due to the small stochastic noise, which is barely visible only in the far tails.

lations are used to recover a natural parameterization of the full self-energy that fulfills the causality principle. This approach allows to control the Monte Carlo noise of the simulation by translating it into a (small) error on the fitted parameters [43].

Results. We perform calculations in the so-called *sc0* framework [51, 52]. This is a standard prescription in nuclear theory that consists in imposing a fully self-consistent calculation for the static component of the self-energy, $\Sigma_p^{(\infty)}$, while the dynamic part is expanded with respect to a mean-field reference propagator. Fig. 3 reports the components $p = 1$ and $p = 6$ of the imaginary part of the irreducible self-energy for $g = 0.3$, $\eta = 0.1$, and $D = 10$. The results were obtained with a Hartree-Fock (HF) reference propagator by sampling ladder diagrams up to order eight. The simulated self-energy shows only small deviations from the exact analytical form, Eq. (3), so that the NLLSM fit is extremely precise.

Our implementation of DiagMC carries three sources of uncertainty. The first is the statistical error that is

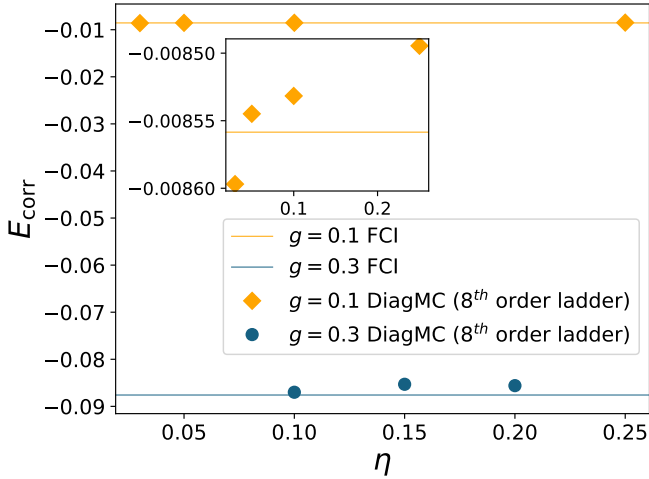


FIG. 4. Correlation energy for different values of the regulator η . The figure shows results for the coupling constants $g = 0.1$ and $g = 0.3$. The solid lines are the full configuration interaction (FCI) results, and they are obtained from the exact diagonalization of the Richardson Hamiltonian.

intrinsic to any Monte Carlo approach and can be controlled to a good extent by additional sampling. Second, we do perform a many-body truncation by restricting our diagram space up to eighth order in PT and to ladder diagrams only. The error involved is negligible because excluded diagram topologies are known to be irrelevant for the Richardson Hamiltonian [27] and the first eight PT orders are substantially converged. The comparison between the NLLSM fit of Eq. (3) and the DiagMC sampling, shown in Fig. 3, demonstrates the quality of our simulations. Finally, we have a dependence on the regulator parameter η [43]. In principle, the exact result is recovered in the limit $\eta \rightarrow 0$, where it would cause numerical instabilities. In fact, however, a finite value of η simply sets the energy resolution of our simulations, and how ‘small’ it should be depends on the specific application. To study the dependence of our results on η we performed simulations using different regulator values in the model space $D = 10$ for $g = 0.1$ and $g = 0.3$. Fig. 4 shows a moderate dependence on the regulator η . The deviation between our calculations and the true correlation energies is at most 1% for both $g = 0.1$ and $g = 0.3$. Hence, we take 1% as the error for all our calculations of correlation energies and always use $\eta = 0.1$.

The correlation energies derived from the Migdal-Galitskii-Koltun (MGK) sum rule [53, 54] are benchmarked against the exact full configuration interaction (FCI) solutions and the ADC(3) many-body truncation values in Fig. 5. The top panel shows the correlation energy dependence on the coupling constant g within the model space of size $D = 10$. The bottom panel shows the correlation energy per particle with changing model space size D , at half-filling, and $g = 0.3$. We find agree-

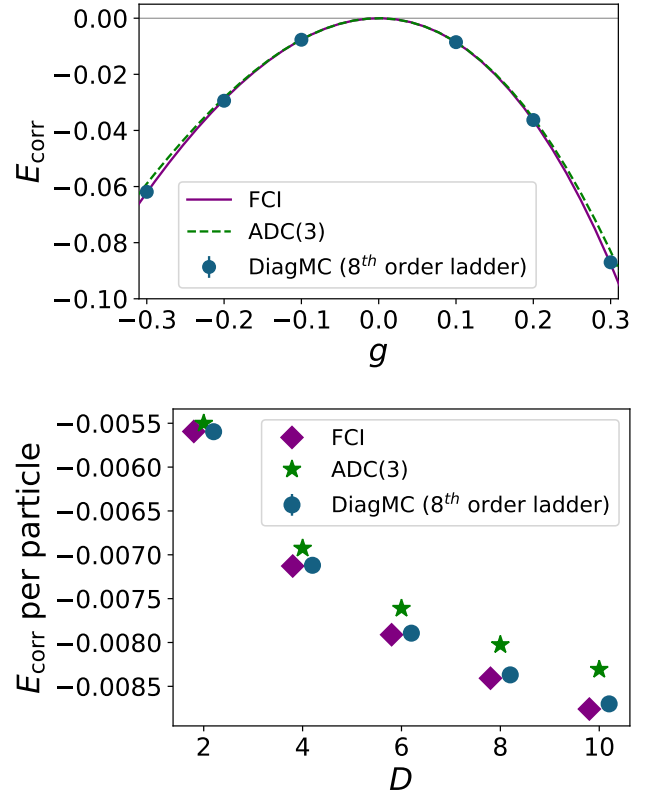


FIG. 5. Correlation energy of the Richardson model at half-filling. The regulator is set at $\eta = 0.1$ and the error of 1% on the correlation energy is too small to be visible in the plot. Top panel: Dependence of the correlation energy on the coupling constant g in the model space $D = 10$. Bottom panel: Correlation energy per particle for different model space dimensions and $g = 0.3$.

ment with the exact energies within the error bars of the Monte Carlo uncertainty, confirming that the present ladder resummation dominates the self-energy expansion. Remarkably, DiagMC with the HF reference propagator outperforms ADC(3). This discrepancy is to be ascribed to the presence of time inversion terms in the ladder series, which is resummed to all orders in ADC(3) but only in a Tamm-Dancoff fashion [27]. DiagMC correctly resums the Feynman ladders, accounting for all possible time orderings.

Conclusion. For the weak-coupling regime, we conclude that DiagMC on bound systems (with discrete spectra) can match and even supersede state-of-the-art methods for computing many-body propagators, including the ADC(3) truncation scheme employed in *ab initio* nuclear physics and quantum chemistry. The Richardson model could be solved without the need to exploit convergence acceleration methods, such as the Borel resummation that has already been widely used by DiagMC applications to condensed matter [55, 56]. This leaves room for approaching more realistic problems. It should be

stressed that this work focused on the Green's function; however, DiagMC can be extended to other methods based on diagrammatic expressions, such as coupled cluster amplitudes or many-body PT contributions. Therefore, DiagMC holds significant potential for advancing various fields of physics involving bound many-fermion systems at zero temperature. The success of the present calculations signifies an initial step towards a unified description of nuclear structure and reactions by performing a stochastic sampling over the space of Feynman diagrams of a simplified pairing Hamiltonian.

* Stefano.Brolli@unimi.it

† Carlo.Barbieri@unimi.it

‡ Enrico.Vigezzi@mi.infn.it

- [1] L. Coraggio, S. Pastore, and C. Barbieri, Editorial: The future of nuclear structure: Challenges and opportunities in the microscopic description of nuclei, *Frontiers in Physics* **8**, 10.3389/fphy.2020.626976 (2021).
- [2] H. Hergert, A guided tour of ab initio nuclear many-body theory, *Frontiers in Physics* **8**, 10.3389/fphy.2020.00379 (2020).
- [3] P. Arthuis, C. Barbieri, M. Vorabbi, and P. Finelli, Ab initio computation of charge densities for Sn and Xe isotopes, *Phys. Rev. Lett.* **125**, 182501 (2020).
- [4] B. Hu, W. Jiang, T. Miyagi, Z. Sun, A. Ekström, C. Forssén, G. Hagen, J. D. Holt, T. Papenbrock, S. R. Stroberg, and I. Vernon, Ab initio predictions link the neutron skin of 208Pb to nuclear forces, *Nat. Phys.* **18**, 1196 (2022).
- [5] A. Ravlic, E. Yüksel, T. Nikšić, and N. Paar, Expanding the limits of nuclear stability at finite temperature, *Nat. Comm.* **14**, 4834 (2023).
- [6] N. Tsunoda, T. Otsuka, K. Takayanagi, N. Shimizu, T. Suzuki, Y. Utsuno, S. Yoshida, and H. Ueno, The impact of nuclear shape on the emergence of the neutron dripline, *Nature* **587**, 66 (2019).
- [7] J. J. Cowan and et al, The impact of nuclear shape on the emergence of the neutron dripline, *Rev. Mod. Phys.* **93**, 015002 (2021).
- [8] J. A. Johnson, Populating the periodic table: nucleosynthesis of the elements, *Science*, 474 (2019).
- [9] H. Sakurai, RIKEN radioactive isotope beam factory project — present status and perspectives, *Pramana* **75**, 369 (2010).
- [10] A. Gade and B. M. Sherrill, NSCL and FRIB at michigan state university: Nuclear science at the limits of stability, *Physica Scripta* **91**, 053003 (2016).
- [11] T. Aumann, Prospects of nuclear structure at the future GSI accelerators, *Progress in Particle and Nuclear Physics* **59**, 3 (2007), international Workshop on Nuclear Physics 28th Course.
- [12] M. Borge, Highlights of the isolde facility and the hie-isolde project, *Nuclear Instruments and Methods in Physics Research Section B: Beam Interactions with Materials and Atoms* **376**, 408 (2016), proceedings of the XVIIth International Conference on Electromagnetic Isotope Separators and Related Topics (EMIS2015), Grand Rapids, MI, U.S.A., 11-15 May 2015.
- [13] S. Gales, Ganil-spiral2: a new era, *Journal of Physics: Conference Series* **267**, 012009 (2011).
- [14] L. M. Jens Dilling, Reiner Krücken, *ISAC and ARIEL: The TRIUMF Radioactive Beam Facilities and the Scientific Program*, 1st ed. (Springer Dordrecht, 2014).
- [15] A. Andrichetto, M. Manziolaro, S. Corradetti, D. Scarpa, A. Monetti, M. Rossignoli, M. Ballan, F. Borgna, F. D'Agostini, F. Gramegna, G. Prete, G. Meneghetti, M. Ferrari, and A. Zenoni, Spes: An intense source of neutron-rich radioactive beams at legnaro, *Journal of Physics: Conference Series* **966**, 012028 (2018).
- [16] C. Hebborn, F. Nunes, G. P. Potel Aguilar, W. H. Dickhoff, J. W. Holt, M. C. Atkinson, R. B. Baker, C. Barbieri, G. Blanchon, M. Burrows, R. Capote Noy, P. Danielewicz, M. Dupuis, C. Elster, J. Escher, L. Hlophe, A. Idini, H. Jayatissa, B. P. Kay, K. Kravvaris, J. J. Manfredi, A. Mercenne, B. Morillon, G. Perdikakis, C. D. Pruitt, G. H. Sargsyan, I. J. Thompson, M. Vorabbi, and T. R. Whitehead, Optical potentials for the rare-isotope beam era, *J. Phys. G* **50**, 060501 (2023).
- [17] S. Baroni, P. Navrátil, and S. Quaglioni, Ab initio description of the exotic unbound ${}^7\text{He}$ nucleus, *Phys. Rev. Lett.* **110**, 022505 (2013).
- [18] J. Rotureau, P. Danielewicz, G. Hagen, G. R. Jansen, and F. M. Nunes, Microscopic optical potentials for calcium isotopes, *Phys. Rev. C* **98**, 044625 (2018).
- [19] A. Idini, C. Barbieri, and P. Navrátil, Ab initio optical potentials and nucleon scattering on medium mass nuclei, *Phys. Rev. Lett.* **123**, 092501 (2019).
- [20] M. Burrows, K. D. Launey, A. Mercenne, R. B. Baker, G. H. Sargsyan, T. Dytrych, and D. Langr, Ab initio translationally invariant nucleon-nucleus optical potentials, *Phys. Rev. C* **109**, 014616 (2024).
- [21] M. Vorabbi, C. Barbieri, V. Somà, P. Finelli, and C. Giusti, Microscopic optical potentials for medium-mass isotopes derived at the first order of watsn multiple-scattering theory, *Phys. Rev. C* **109**, 034613 (2024).
- [22] F. Capuzzi and C. Mahaux, Projection operator approach to the self-energy, *Annals of Physics* **245**, 147 (1996).
- [23] L. Cederbaum, Optical potentials and propagators for elastic and inelastic scattering from many-body targets, *Annals of Physics* **291**, 169 (2001).
- [24] J. Escher and B. K. Jennings, One-body overlap functions, equations of motion, and phenomenological potentials, *Phys. Rev. C* **66**, 034313 (2002).
- [25] W. Dickhoff and D. Van Neck, *Many-body theory exposed!: Propagator description of quantum mechanics in many-body systems* (World Scientific, 2005).
- [26] C. Mahaux, Microscopic theories of atomic and nuclear optical potentials, in *Recent Progress in Many-Body Theories: Volume 4* (Springer US, Boston, MA, 1995) pp. 171–175.
- [27] C. Barbieri and A. Carbone, Self-Consistent Green's Function Approaches, in *An Advanced Course in Computational Nuclear Physics*, Lecture Notes in Physics, Vol. 936 (Springer, 2017) Chap. 11, pp. 571–644.
- [28] F. Raimondi and C. Barbieri, Algebraic diagrammatic construction formalism with three-body interactions, *Phys. Rev. C* **97**, 054308 (2018).
- [29] N. V. Prokof'ev and B. V. Svistunov, Polaron Problem by Diagrammatic Quantum Monte Carlo, *Phys. Rev. Lett.* **81**, 2514 (1998).

- [30] N. V. Prokof'ev and B. V. Svistunov, Bold diagrammatic Monte Carlo: A generic sign-problem tolerant technique for polaron models and possibly interacting many-body problems, *Phys. Rev. B* **77**, 125101 (2008).
- [31] K. Van Houcke, F. Werner, T. Ohgoe, N. V. Prokof'ev, and B. V. Svistunov, Diagrammatic Monte Carlo algorithm for the resonant fermi gas, *Phys. Rev. B* **99**, 035140 (2019).
- [32] K. Van Houcke, F. Werner, E. Kozik, N. Prokof'ev, B. Svistunov, M. J. H. Ku, A. T. Sommer, L. W. Cheuk, A. Schirrotzek, and M. W. Zwierlein, Feynman diagrams versus fermi-gas feynman emulator, *Nature Physics* **8**, 366 (2012).
- [33] K. Haule and K. Chen, Single-particle excitations in the uniform electron gas by diagrammatic monte carlo, *Sci. Rep.* **12**, 2294 (2022).
- [34] K. Chen and K. Haule, A combined variational and diagrammatic quantum Monte Carlo approach to the many-electron problem, *Nat. Commun.* **10**, 3725 (2019).
- [35] M. Vanhoecke and M. Schirò, Diagrammatic monte carlo for dissipative quantum impurity models, *Phys. Rev. B* **109** (2024).
- [36] S. D. Baerdemacker, V. Hellemans, R. van den Berg, J.-S. Caux, K. Heyde, M. V. Raemdonck, D. V. Neck, and P. A. Johnson, Probing pairing correlations in sn isotopes using richardson-gaudin integrability, *Journal of Physics: Conference Series* **533**, 012058 (2014).
- [37] R. W. Richardson, Application to the exact theory of the pairing model to some even isotopes of lead, *Physics Letters* **5**, 82 (1963).
- [38] P. A. Johnson, C. E. Fecteau, F. Berthiaume, S. Cloutier, L. Carrier, M. Gratton, P. Bultinck, S. De Baerdemacker, D. Van Neck, P. Limacher, and P. W. Ayers, Richardson-gaudin mean-field for strong correlation in quantum chemistry, *The Journal of Chemical Physics* **153**, 104110 (2020).
- [39] M. Hjorth-Jensen, M. P. Lombardo, and U. van Kolck, eds., *An Advanced Course in Computational Nuclear Physics*, Lecture Notes in Physics, Vol. 936 (Springer, 2017).
- [40] M. Rigo, B. Hall, M. Hjorth-Jensen, A. Lovato, and F. Pederiva, Solving the nuclear pairing model with neural network quantum states, *Phys. Rev. E* **107**, 025310 (2023).
- [41] M. Companys Franzke, A. Tichai, K. Hebeler, and A. Schwenk, Eigenvector continuation for the pairing hamiltonian, *Phys. Rev. C* **109**, 024311 (2024).
- [42] R. W. Richardson, A restricted class of exact eigenstates of the pairing-force hamiltonian, *Physics Letters* **3**, 277 (1963).
- [43] See Supplemental Material at `URL_will_be_inserted_by_publisher` for details about the Richardson model, the fundamental equations of DiagMC, and the error induced by the finite regulator and the Monte Carlo stochastic process.
- [44] S. Brolli, *A Diagrammatic Monte Carlo Method for a Fermionic Pairing Model*, Master's thesis, Università degli Studi di Milano (2023).
- [45] C. Drischler, K. Hebeler, and A. Schwenk, Chiral interactions up to next-to-next-to-next-to-leading order and nuclear saturation, *Phys. Rev. Lett.* **122**, 042501 (2019).
- [46] P. Arthuis, T. Duguet, A. Tichai, R.-D. Lasserri, and J.-P. Ebran, ADG: Automated generation and evaluation of many-body diagrams I. Bogoliubov many-body perturbation theory, *Computer Physics Communications* **240**, 202 (2019).
- [47] N. Metropolis, A. W. Rosenbluth, M. N. Rosenbluth, A. H. Teller, and E. Teller, Equation of state calculations by fast computing machines, *The Journal of Chemical Physics* **21**, 1087 (1953), <https://doi.org/10.1063/1.1699114>.
- [48] W. K. Hastings, Monte Carlo sampling methods using Markov chains and their applications, *Biometrika* **57**, 97 (1970), <https://academic.oup.com/biomet/article-pdf/57/1/97/23940249/57-1-97.pdf>.
- [49] J. Schirmer, *Many-Body Methods for Atoms, Molecules and Clusters* (Springer International Publishing, Cham, 2018).
- [50] J. Schirmer, L. S. Cederbaum, and O. Walter, New approach to the one-particle green's function for finite fermi systems, *Phys. Rev. A* **28**, 1237 (1983).
- [51] V. Somà, C. Barbieri, and T. Duguet, Ab initio self-consistent gorkov-green's function calculations of semi-magic nuclei: Numerical implementation at second order with a two-nucleon interaction, *Phys. Rev. C* **89**, 024323 (2014).
- [52] C. Barbieri, T. Duguet, and V. Somà, Gorkov algebraic diagrammatic construction formalism at third order, *Phys. Rev. C* **105**, 044330 (2022).
- [53] V. M. Galitskii and A. B. Migdal, Application of quantum field theory methods to the many body problem, *Sov. Phys. JETP* **7**, 18 (1958).
- [54] D. S. Koltun, Theory of mean removal energies for single particles in nuclei, *Phys. Rev. C* **9**, 484 (1974).
- [55] K. V. Houcke, E. Kozik, N. Prokof'ev, and B. Svistunov, Diagrammatic Monte Carlo, *Physics Procedia* **6**, 95 (2010), *Computer Simulations Studies in Condensed Matter Physics XXI*.
- [56] R. Rossi, T. Ohgoe, K. Van Houcke, and F. Werner, Resummation of diagrammatic series with zero convergence radius for strongly correlated fermions, *Phys. Rev. Lett.* **121**, 130405 (2018).

SUPPLEMENTAL MATERIAL

Exact solution of the Richardson model

The Richardson Hamiltonian has an exact analytic solution [1]. For P pairs of fermions, this is

$$|\Psi_{g.s.}^{2P}\rangle = \prod_{i=1}^P b_i^\dagger |0\rangle, \quad (\text{S1})$$

where

$$b_i^\dagger = \sum_{p=1}^D \frac{1}{2(p-1) - E_i} c_{p\uparrow}^\dagger c_{p\downarrow}^\dagger \quad (\text{S2})$$

and the parameters E_i are the D solutions of the equations

$$1 - \frac{g}{2} \sum_{p=1}^D \frac{1}{2(p-1) - E_i} - g \sum_{j \neq i}^P \frac{1}{E_i - E_j} = 0 \quad \forall i = 1, \dots, D \quad (\text{S3})$$

The exact ground state energy is given by

$$E_{GS} = \sum_{i=1}^P E_i, \quad (\text{S4})$$

where E_i are the P lowest energy solutions.

Basic DiagMC formalism

Diagrammatic Monte Carlo (DiagMC) is based on the Dyson equation approach to the Green's function. The self-energy Σ^* is given by all one-particle irreducible Feynman diagrams¹. In the self-consistent approach, the self-energy expansion is further reduced by including only skeleton diagrams, and hence DiagMC must sample one-particle irreducible skeleton diagrams. We build our DiagMC extension to the Richardson model building upon the formalism set in Ref. [2]. To simplify the notation, we will assume spin-up unless otherwise specified, and define all one-body quantities as $O_p := O_{p\uparrow, p\uparrow}$.

The self-energy is given by

$$\Sigma_p^*(\omega) = \sum_{\mathcal{T}} \sum_{q_1, \dots, q_n} \int d\omega_1 \dots d\omega_m \mathcal{D}_p(\omega; \mathcal{T}, q_1 \dots q_n, \omega_1 \dots \omega_m) 1_{\mathcal{T} \in S_{\Sigma^*}}, \quad (\text{S5})$$

where \mathcal{D} is a diagram with topology \mathcal{T} , internal single-particle quantum numbers $q_1 \dots q_n$, and internal frequencies $\omega_1 \dots \omega_m$. The characteristic function $1_{\mathcal{T} \in S_{\Sigma^*}}$ selects one-particle irreducible, skeleton topologies. Due to its analytic form, we expect the self-energy to be appreciably different from zero over a finite interval of energies ω . We can divide this interval into bins and expand inside each bin $[\omega_i, \omega_{i+1}]$ over a basis $\{B_n(\omega)\}_{n=0}^\infty$. We choose the complete orthonormal basis

$$B_n(\omega) = \sqrt{\frac{2n+1}{\omega_{i+1} - \omega_i}} L_n \left(\frac{2}{\omega_{i+1} - \omega_i} (\omega - \omega_i) - 1 \right) \quad n = 0, 1, 2, \dots \quad (\text{S6})$$

¹A diagram is said to be one-particle irreducible if it cannot be separated into two distinct diagrams by cutting one propagator line.

where $L_n(x)$ is the n -th Legendre polynomial. Since the order n is also the number of nodes, a high-order expansion would introduce a strong source of sign problem. Accordingly, we truncate the expansion at $n_{max} = 2$ and adapt the size of for each bin to avoid significant oscillations inside the interval. From the exact analytic form of the self-energy we can estimate the width of the Lorentzians to be of the order of the regulator η . Hence, bins of dimension $\approx \eta$ ensure an accurate low-order truncation. To avoid a large number of bins for small values of η , one can use an adaptive mesh in which the intervals near the Lorentzian peaks have size $\approx \eta$, while all other bins are much larger, even of the order of a few tens of energy units. A preliminary computation with large intervals and few samples would suffice to estimate the pole position and the optimal mesh. For the present work, it wasn't necessary to adopt this refinement because the number of self-energy poles is limited².

The self-energy expansion on the basis (S6) gives

$$\Sigma_p^*(\omega) = \sum_{n=0}^{+\infty} \Sigma_p^{(n)} B_n(\omega) \approx \sum_{n=0}^2 \Sigma_p^{(n)} B_n(\omega), \quad (\text{S7})$$

with

$$\Sigma_p^{(n)} = \int_{\omega_i}^{\omega_{i+1}} d\omega B_n(\omega) \Sigma_p^*(\omega). \quad (\text{S8})$$

The DiagMC simulation calculates the coefficients (S8) inside each bin for every p and allows reconstructing the self-energy through equation (S7).

We can substitute (S5) into (S8), and using the shorthand notation $\mathcal{C} := (\mathcal{T}, q_1, \dots, q_n, \omega_1, \dots, \omega_m)$ we get

$$\Sigma_p^{(n)} = \int_{\omega_i}^{\omega_{i+1}} d\omega \int d\mathcal{C} B_n(\omega) \mathcal{D}_p(\omega; \mathcal{C}) 1_{\mathcal{T} \in S_{\Sigma^*}}. \quad (\text{S9})$$

The main idea of DiagMC is to rewrite this expansion as a weighted average over a probability distribution function w_p . Choosing w_p to be independent of n allows us to evaluate the coefficients $\Sigma_p^{(n)}$ for every n with a single simulation instead of performing separate samplings for each n up to n_{max} . We still require a different simulation for every basis-state level $p = 1, \dots, D$. To this end, we rewrite (S9) as

$$\Sigma_p^{(n)} = Z_p \int_{\omega_i}^{\omega_{i+1}} d\omega \int d\mathcal{C} \frac{|\mathcal{D}_p(\omega; \mathcal{C})|}{Z_p} \exp[i \arg \mathcal{D}_p(\omega; \mathcal{C})] B_n(\omega) 1_{\mathcal{T} \in S_{\Sigma^*}}, \quad (\text{S10})$$

where Z_p is a normalization factor given by

$$Z_p := \int_{\omega_i}^{\omega_{i+1}} d\omega \int d\mathcal{C} |\mathcal{D}_p(\omega; \mathcal{C})|. \quad (\text{S11})$$

We can define the probability distribution function as

$$w_p(\omega; \mathcal{C}) := \frac{|\mathcal{D}_p(\omega; \mathcal{C})|}{Z_p} \quad (\text{S12})$$

and rewrite Eq. (S10) as

$$\Sigma_p^{(n)} = Z_p \int_{\omega_i}^{\omega_{i+1}} d\omega \int d\mathcal{C} w_p(\omega; \mathcal{C}) \exp[i \arg \mathcal{D}_p(\omega; \mathcal{C})] B_n(\omega) 1_{\mathcal{T} \in S_{\Sigma^*}}. \quad (\text{S13})$$

²For $D = 10$ there are five closeby poles.

If we can sample diagrams $\{\mathcal{D}_p(\omega_j; \mathcal{C}_j)\}_{j=1}^N$ according to the probability distribution function (S12), we can calculate (S13) with

$$\Sigma_p^{(n)} = Z_p \lim_{N \rightarrow \infty} \frac{1}{N} \sum_{j=1}^N \exp[i \arg \mathcal{D}_p(\omega_j; \mathcal{C}_j)] B_n(\omega_j) 1_{\mathcal{T}_j \in S_{\Sigma^*}}. \quad (\text{S14})$$

The normalization factor Z_p is estimated during the DiagMC simulation by selecting a subset of diagrams $S_{\mathcal{N}}$, called normalization sector, with a known weight $Z_p^{\mathcal{N}}$. Since

$$Z_p^{\mathcal{N}} := \int_{\omega_i}^{\omega_{i+1}} d\omega \int_{\mathcal{T} \in S_{\mathcal{N}}} d\mathcal{C} |\mathcal{D}_p(\omega; \mathcal{C})|, \quad (\text{S15})$$

we can estimate the normalization factor by counting the number of times these diagrams are sampled. If the number of visits to the normalization sector is \mathcal{N} , the probability distribution function (S12) implies

$$\lim_{N \rightarrow \infty} \frac{\mathcal{N}}{N} = \frac{Z_p^{\mathcal{N}}}{Z_p} \quad (\text{S16})$$

and Eq. (S14) becomes

$$\Sigma_p^{(n)} = Z_p^{\mathcal{N}} \lim_{N \rightarrow \infty} \frac{1}{\mathcal{N}} \sum_{j=1}^N \exp[i \arg \mathcal{D}_p(\omega_j; \mathcal{C}_j)] B_n(\omega_j) 1_{\mathcal{T}_j \in S_{\Sigma^*}}. \quad (\text{S17})$$

We discuss the normalization sector in depth in the next subsection.

Hartree-Fock and normalization sector

The Hartree-Fock diagram in Fig. S1 has the analytic expression

$$\mathcal{D}_p^{\text{HF}} = i \frac{g}{2} \int_{-\infty}^{\infty} \frac{d\omega_1}{2\pi} G_{p\downarrow p\downarrow}(\omega_1) e^{i\omega_1 \epsilon} = i \frac{g}{2} \int_{-\infty}^{\infty} \frac{d\omega_1}{2\pi} G_p(\omega_1) e^{i\omega_1 \epsilon}, \quad (\text{S18})$$

where the last equality is due to the spin-up - spin-down symmetry.

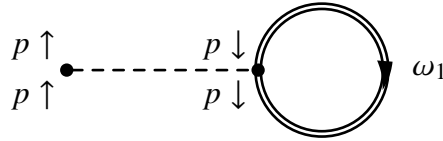


FIG. S1. First-order (tadpole) diagram. This diagram accounts for the static part of the self-energy [3].

Eq. (S18) is difficult to calculate with DiagMC due to the infinitesimal ϵ that needs to be taken to 0^+ after the integral. Thus, we compute the result analytically from

$$\mathcal{D}_p^{\text{HF}} = -\frac{g}{2} \sum_k |\langle \Psi_k^{2P-1} | c_p | \Psi_{g.s.}^{2P} \rangle|^2. \quad (\text{S19})$$

Eq. (S19) is the total static self-energy. To avoid the problems of Eq. (S18), we calculate the static self-energy exactly through Eq. (S19) and simulate the dynamic self-energy with DiagMC. This is equivalent to considering S_{Σ^*} in (S17) as the subset of skeleton diagrams of order greater than 1.

Since the Hartree-Fock diagram has been removed from the set of sampled diagrams, and we include only skeleton diagrams in the self-energy simulation, we can redefine the self-closing propagator to

$$\tilde{G}_p(\omega_1) = \frac{iA\gamma}{\omega_1^2 + \gamma^2}, \quad (\text{S20})$$

with $A, \gamma > 0$. The redefined self-closing propagator will be drawn as a zigzag line, as shown in Fig. S2. This substitution allows us to take the limit $\epsilon \rightarrow 0^+$ before performing the integral.

The redefinition of the HF diagram allows the manipulation of the weight (and hence the amount of sampling) of the diagram. This is a useful feature to keep under control the normalization sector. Hence, we take as normalization sector $S_{\mathcal{N}}$ the HF diagram in Fig. S1, with the closed propagator replaced by the unphysical zigzag propagator (S20). The weight of the normalization sector is found analytically from Eq. (S15)

$$Z_p^{\mathcal{N}} = \frac{|g|}{2} \int_{\omega_i}^{\omega_{i+1}} d\omega \int_{-\infty}^{+\infty} \frac{d\omega_1}{2\pi} \frac{A\gamma}{\omega_1^2 + \gamma^2} = \frac{|g|}{4} A\Delta\omega := Z^{\mathcal{N}}, \quad (\text{S21})$$

which is independent of p and where $\Delta\omega := \omega_{i+1} - \omega_i$. The parameters A and γ can be adjusted to optimize the sampling of normalization diagrams. It was sufficient to choose $\gamma \approx 15$ and $A \approx 3$ throughout this work, although they could be fine-tuned according to the coupling constant g , the model space dimension, and the order of the perturbative expansion.

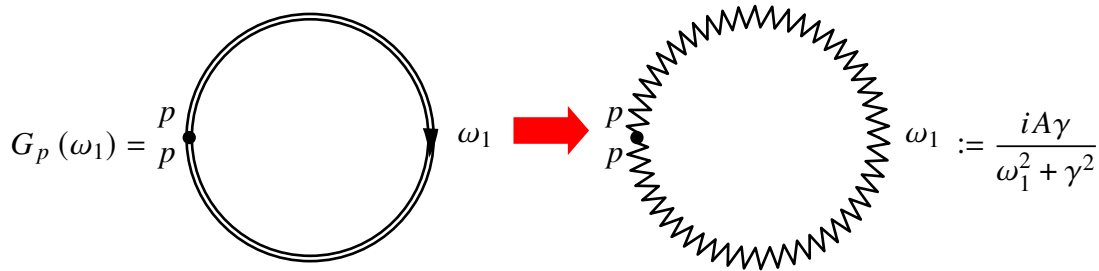


FIG. S2. Self-closing physical and unphysical propagators. The self-closing physical propagator (represented by a double solid line) is replaced with an unphysical propagator (represented by a zigzag line) with an arbitrarily chosen value.

Updates

Eq. (S17) implies sampling the space of Feynman diagram topologies. While this includes all skeleton diagrams of order greater than one, the diagrammatic expansion of the Richardson model is dominated by ladder diagrams. Here, we limit ourselves to this subset and sample diagrams up to order eight. The same algorithm can be pushed to higher-order contributions without modifications. We perform a Markov chain in the space of topologies, quantum numbers, and frequencies. The first diagram of the Markov chain is taken as the normalization diagram. The following diagrams are proposed by randomly choosing one of five possible updates that modify the diagram at the previous step. To reproduce the correct probability distribution function (S12), we accept or reject the update according to Metropolis-Hastings algorithm [4, 5]. The updates we used to sample ladder contributions are as follows:

- *Change of ω*

This update changes the external frequency ω of the diagram. To preserve frequency conservation, we change the frequency of the backward-going propagator as in Fig. S3.

The new frequency ω' is chosen according to a uniform distribution in the bin $[\omega_i, \omega_{i+1}]$ and the Metropolis-Hastings acceptance ratio is

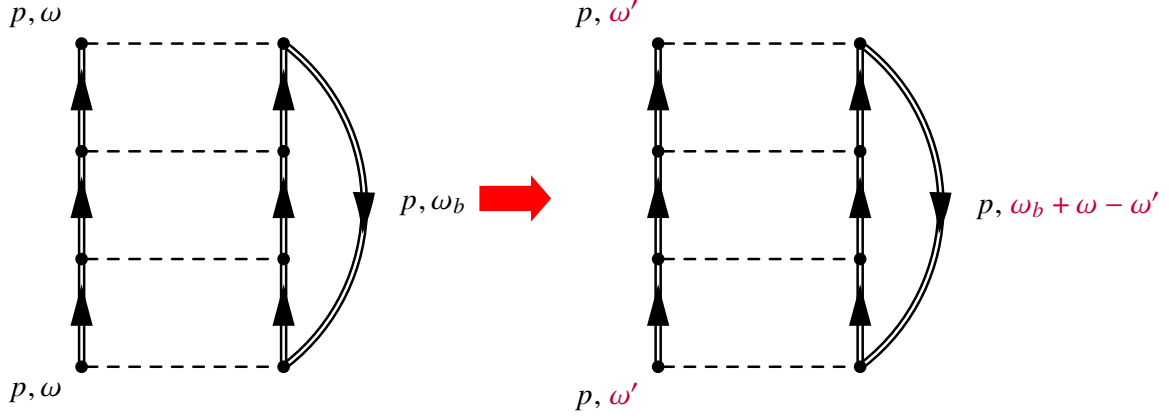


FIG. S3. Update *Change* ω .

$$q_\omega = \frac{|G_p(\omega_b + \omega - \omega')|}{|G_p(\omega_b)|}. \quad (\text{S22})$$

- *Change of the internal frequencies*

This update changes the frequency ω_b of the backward-going propagator that connects the two ends of the ladder. We choose the new frequency ω'_b according to a Lorentzian distribution $L(\omega)$ centered around zero with width γ . The Lorentzian is particularly suitable because it samples high-frequency contributions with good statistics. This is important because the propagator has asymptotic behavior $\sim \frac{1}{\omega}$ for $\omega \rightarrow \infty$. The propagators on the left-hand side of the ladder diagram have their frequency ω_i changed to $\omega_i - \omega_b + \omega'_b$. The update is shown in Fig. S4.

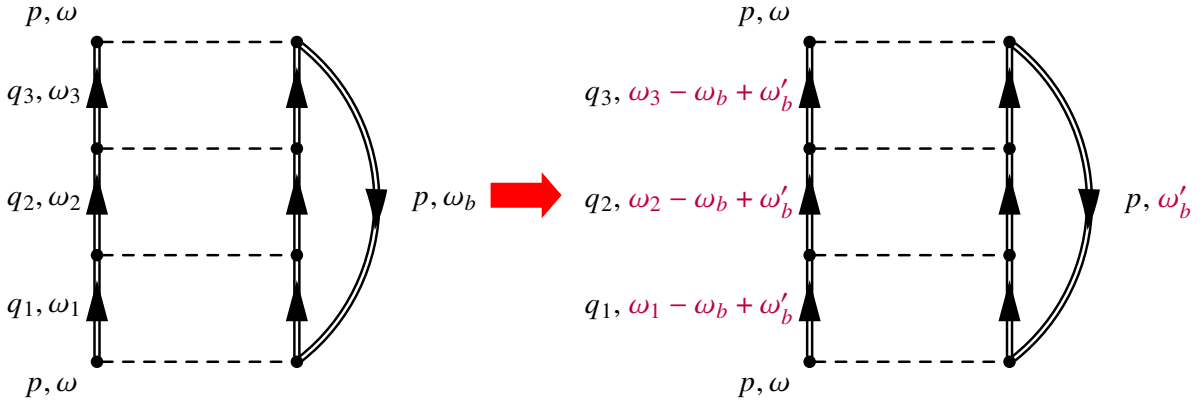


FIG. S4. Update *Change of the internal frequencies*.

The acceptance ratio of the update is

$$q_{\omega \text{ int}} = \frac{L(\omega_b) |G_p(\omega'_b)|}{L(\omega'_b) |G_p(\omega_b)|} \prod_{j=1}^{\text{order}-1} \frac{|G_{q_j}(\omega_j - \omega_b + \omega'_b)|}{|G_{q_j}(\omega_j)|}. \quad (\text{S23})$$

Notice that this is the only update that can move over the entire real axis the frequency of the backward-going propagator connecting the two ends of the ladder. This is in contrast to the update *Change* ω , which can only change ω_b by an amount within the interval $[\omega_i, \omega_{i+1}]$. This update is needed to perform the integration over ω_b .

- *Change of single particle quantum numbers and frequencies*

This update chooses a random propagator on the left-hand side of the ladder and proposes to change its frequency and single-particle quantum number. The new frequency is sampled from the same Lorentzian distribution of the update *Change of the internal frequencies*. The new single-particle quantum number is drawn from a uniform probability distribution on the integers $[1, D]$. The propagator on the right-hand side has its frequency changed to conserve the total frequency. The single-particle quantum number on the right-hand side is also changed to match the one on the left, as required by the particular form of the interaction.

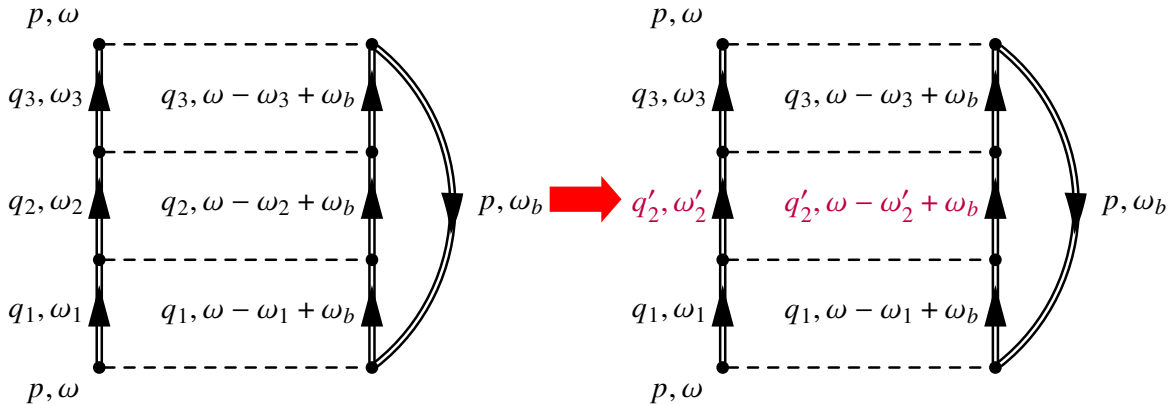


FIG. S5. Update *Change single particle quantum numbers and frequencies*. We assumed that the random propagator chosen was the second from the bottom appearing on the left-hand side of the ladder.

This update is depicted in Fig. S5 and its ratio is

$$q_{q,\omega} = \frac{L(\omega_2) |G_{q'_2}(\omega'_2) G_{q'_2}(\omega - \omega'_2 + \omega_b)|}{L(\omega'_2) |G_{q_2}(\omega_2) G_{q_2}(\omega - \omega_2 + \omega_b)|}. \quad (\text{S24})$$

- *Add/Remove Rung*

The *Add/Remove Rung* updates are a pair of complementary updates that propose to add (remove) a pair of propagators to (from) the top of the diagram. When called on the normalization diagram, the *Add Rung* update proposes to turn it into the second-order ladder, while *Remove Rung* is always rejected. When *Remove Rung* is called upon the second-order diagram, it proposes returning to the normalization sector. Accordingly, the backward-going propagator that connects the ends of the ladder is changed into the unphysical propagator of Fig. S2, and vice-versa when moving to the second-order ladder diagram. The simulations are performed with an order cutoff implemented by rejecting the *Add Rung* update when called on diagrams of the maximum order. We show the update in Fig. S6. The frequency on the left-hand side of the top pair is drawn from the same Lorentzian function $L(\omega)$ of the other updates, and the frequency of the right propagator is adjusted to preserve frequency conservation. The single-particle quantum number is chosen randomly among the integers $[1, D]$.

The update ratio of the *Add Rung* depicted in Fig. S6 is

$$q_{AL} = \frac{|g|}{4\pi} \frac{D}{L(\omega_3)} |G_{q_3}(\omega_3) G_{q_3}(\omega - \omega_3 + \omega_b)|, \quad (\text{S25})$$

while for the *Remove Rung* it is

$$q_{RL} = \frac{1}{q_{AL}}. \quad (\text{S26})$$

The updates presented can sample all ladder diagrams ergodically up to arbitrarily high orders.

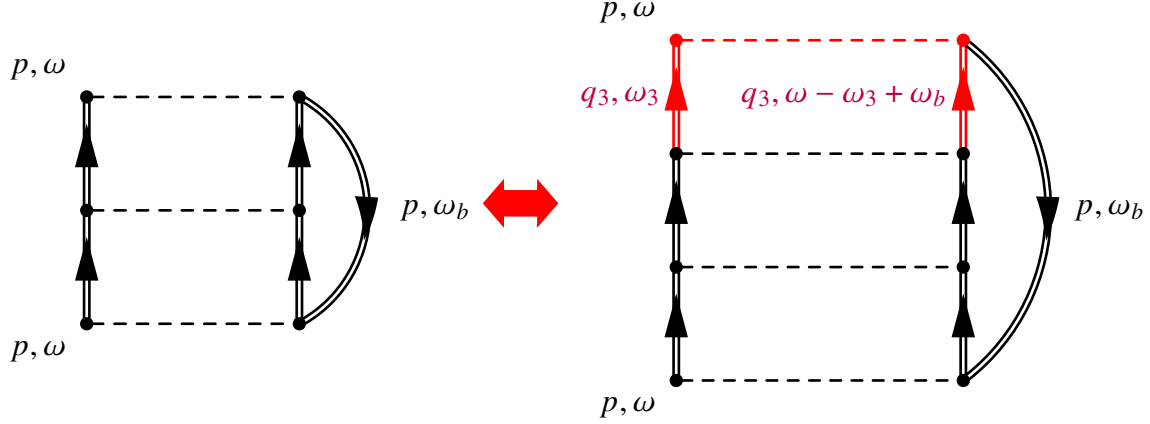


FIG. S6. Update *Add/Remove Rung*. The example in the picture shows the second and third-order ladder diagrams.

Dyson matrix diagonalization

DiagMC calculates the coefficients (S8) of the self-energy expansion, Eq. (S7). The causality principle constrains the full form of the dynamic self-energy by its imaginary part. Consequently, we can focus on the imaginary part of the self-energy and perform a non-linear least-square minimization to fit the imaginary part of the self-energy as a sum of Lorentzian functions. The functional form of the fit is motivated by the exact analytic form of the self-energy given by equation. The representation is generally broken by perturbation theory, however, if the coupling constant lies within the convergence radius of the series expansion, the perturbative expansion must approach the analytic form of the exact self-energy. We focus on this small coupling regime. If the regulator η of the propagator is finite, the imaginary part of the self-energy goes from being a sum of Dirac δ functions [3] to a sum of Lorentzian functions with finite width,

$$\text{Im} [\Sigma_p^*(\omega)] = \sum_j \frac{\pm C_p^j A_p^j}{(\omega - B_p^j)^2 + C_p^{j2}}, \quad (\text{S27})$$

where $A_p^j, C_p^j > 0$ and the overall sign is + (-) for hole (particle) poles. Each Lorentzian has three free parameters: the strength A_p^j , the centroid B_p^j , and the width C_p^j . This set of parameters, combined with the static self-energy given by the HF diagram, gives the full self-energy

$$\Sigma_p^*(\omega) = \Sigma_p^\infty + \sum_j \frac{A_p^j}{\omega - B_p^j \mp iC_p^j}. \quad (\text{S28})$$

This form lets us take the limit $C_p^j \rightarrow 0^+$. The dependence on the regulator is suppressed in the explicit expression of the self-energy, however, it is still hidden in the parameters A_p^j and B_p^j .

The exact analytic form of the propagator is

$$G_p(\omega) = \sum_j \frac{|\mathcal{Z}_p^j|^2}{\omega - \varepsilon_j^\pm \pm i\eta}, \quad (\text{S29})$$

where \mathcal{Z}_p^j are the overlap amplitudes for quasiparticle (ε_j^+) and quasihole (ε_j^-) solutions.

We can find the poles and residues of the propagator by solving the Dyson equation. This equation can be recast into a standard eigenvalue problem [6]. We can further exploit the diagonal nature of the propagator to divide the eigenvalue problem into D smaller eigenvalue problems of the form

$$\begin{pmatrix} p-1 + \Sigma_p^\infty & \sqrt{A_p^1} & \sqrt{A_p^2} & \dots & \sqrt{A_p^N} \\ \sqrt{A_p^1} & B_p^1 & 0 & \dots & 0 \\ \sqrt{A_p^2} & 0 & B_p^2 & \dots & 0 \\ \vdots & \vdots & \vdots & \ddots & \vdots \\ \sqrt{A_p^N} & 0 & 0 & \dots & B_p^N \end{pmatrix} \begin{pmatrix} Z_p^j \\ W^1 \\ W^2 \\ \vdots \\ W^N \end{pmatrix} = \varepsilon_j^\pm \begin{pmatrix} Z_p^j \\ W^1 \\ W^2 \\ \vdots \\ W^N \end{pmatrix} \quad (\text{S30})$$

with $p = 1, \dots, D$. To determine whether a pole is particle-like or hole-like we look at the position of its energy ε_j^\pm with respect to the Fermi energy. We compute the Fermi energy by requiring that the total sum of spectroscopic factors over the quasihole states is equal to the number of particles. Eq. (S30), complemented with the normalization condition

$$|Z_p^j|^2 + \sum_{k=1}^N |W^k|^2 = 1, \quad (\text{S31})$$

fully determines the propagator.

Convergence of the perturbation series

To determine the convergence of the ladder expansion we computed the exact ladder resummation, and then we performed DiagMC calculations at increasing ladder order. Fig. S7 shows the imaginary part of the component $p = 1$ of the self-energy. The self-energy was calculated in the model space of size $D = 10$ for the coupling constant $g = 0.3$ and regulator $\eta = 0.1$. The perturbation expansion is approaching the exact resummation as the order increases and it reaches convergence at the 8-th order.

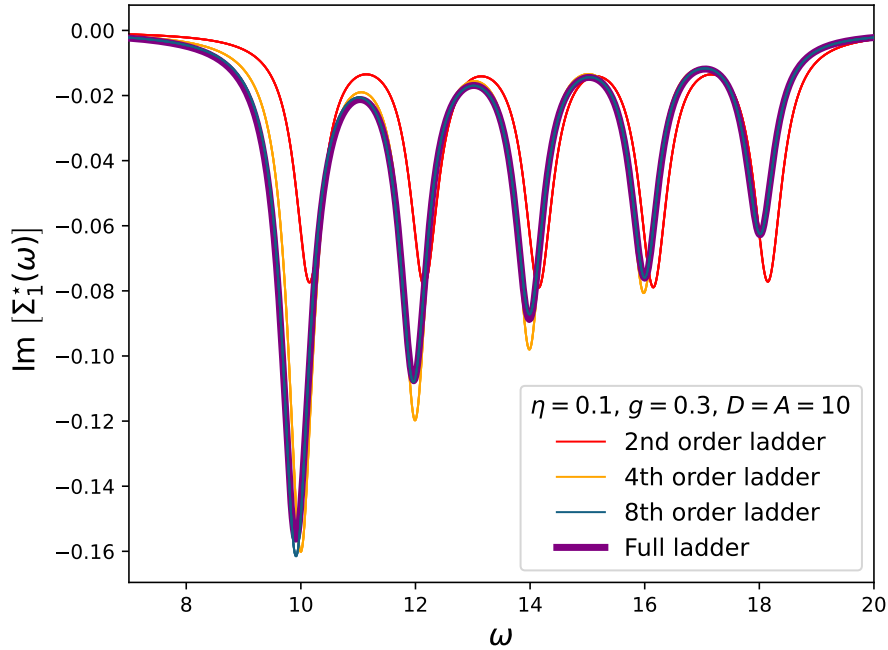


FIG. S7. Imaginary part of the component $p = 1$ of the self-energy. The values of the parameters of the calculation are $g = 0.3$, $\eta = 0.1$ and $D = 10$.

Error determination

Our DiagMC implementation produces an error on the fitted parameters given by a combination of the stochastic Monte Carlo error, the error due to a sharp truncation at order eight of the ladder expansion, and the use of a finite regulator. The latter has been studied in detail in the main text. In this section we focus on the uncertainty on the parameters of the fit once the regulator has been fixed. The uncertainty on the parameters, σ , is defined so that a deviation of $\pm 1\sigma$ corresponds to an increase in the total chi-squared (χ^2) by the reduced chi-squared (χ_{red}^2) from its minimum value. For each parameter, we assume a Gaussian distribution with standard deviation σ and mean value given by the best-fit result. We then sample values of A_p^j and B_p^j from this distribution and solve the Dyson matrix eigenproblem of Eq. (S30). Repeating this process $\sim 10^4$ times, we get a convergent standard deviation for the final correlation energy. We found this error to be an order of magnitude smaller than the one induced by the regulator.

A further (more qualitative) check on the error of our stochastic simulations can be performed by looking at the computed spectral function. Fig. S8 shows the case for $g = 0.3$ and $D = 10$. There are 10 dominant peaks (5 quasiholes and 5 quasiparticles) that account for almost all of the spectral strength (showing that the Richardson model is only weakly fragmented) and 50 smaller peaks, induced by the correlations. Our DiagMC implementation accurately reproduces the particle-hole symmetry of the spectral function around the Fermi energy. Such an accurate result is possible due to the small stochastic noise of our simulations.

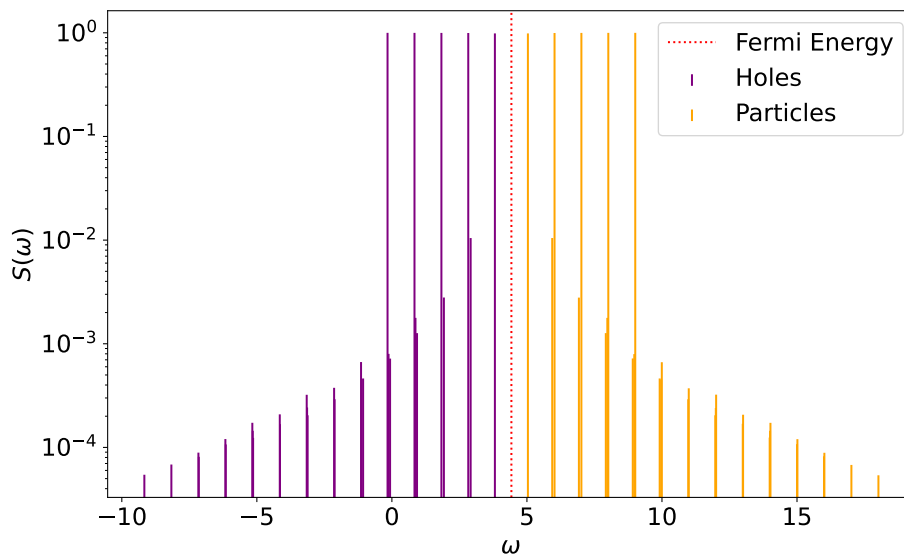


FIG. S8. Spectral function of the Richardson model. We show results obtained in a model space of dimension $D = 10$ at half filling and $g = 0.3$, $\eta = 0.1$. The spectral function is calculated at the eight-order ladder expansion with DiagMC and a HF reference propagator in the *sc0* scheme.

-
- [1] R. W. Richardson, A restricted class of exact eigenstates of the pairing-force hamiltonian, *Physics Letters* **3**, 277 (1963).
- [2] K. Van Houcke, F. Werner, T. Ohgoe, N. V. Prokof'ev, and B. V. Svistunov, Diagrammatic monte carlo algorithm for the resonant fermi gas, *Phys. Rev. B* **99**, 035140 (2019).
- [3] W. Dickhoff and D. Van Neck, *Many-body theory exposed!: Propagator description of quantum mechanics in many-body systems* (World Scientific, 2005).
- [4] N. Metropolis, A. W. Rosenbluth, M. N. Rosenbluth, A. H. Teller, and E. Teller, Equation of state calculations by fast computing machines, *The Journal of Chemical Physics* **21**, 1087 (1953), <https://doi.org/10.1063/1.1699114>.
- [5] W. K. Hastings, Monte Carlo sampling methods using Markov chains and their applications, *Biometrika* **57**, 97 (1970), <https://academic.oup.com/biomet/article-pdf/57/1/97/23940249/57-1-97.pdf>.
- [6] C. Barbieri and A. Carbone, Self-Consistent Green's Function Approaches, in *An Advanced Course in Computational Nuclear Physics*, *Lecture Notes in Physics*, Vol. 936 (Springer, 2017) Chap. 11, pp. 571–644.